PNAS RESEARCH ARTICLE | BIOPHYSICS AND COMPUTATIONAL BIOLOGY

Architecture of the Sap S-layer of *Bacillus anthracis* revealed by integrative structural biology

Adrià Sogues[a,b,1], Kendra Leigh[c,d,e,f,1], Ethan V. Halingstad[g,1], Sander E. Van der Verren[a,b,1], Adam J. Cecil[g], Antonella Fioravanti[a,b], Alexander J. Pak[g,h,i], Misha Kudryashev[c,d,e,f,2], and Han Remaut[a,b,2]

Affiliations are included on p. 10.

Edited by Axel Brunger, Stanford University, Stanford, CA; received August 2, 2024; accepted October 28, 2024

Bacillus anthracis **is a spore-forming gram-positive bacterium responsible for anthrax, an infectious disease with a high mortality rate and a target of concern due to bioterrorism and long-term site contamination. The entire surface of vegetative cells in exponential or stationary growth phase is covered in proteinaceous arrays called S-layers, composed of Sap or EA1 protein, respectively. The Sap S-layer represents an important virulence factor and cell envelope support structure whose paracrystalline nature is essential for its function. However, the spatial organization of Sap in its lattice state remains elusive. Here, we employed cryoelectron tomography and subtomogram averaging to obtain a map of the Sap S-layer from tubular polymers that revealed a conformational switch between the postassembly protomers and the previously available X-ray structure of the condensed monomers. To build and validate an atomic model of the lattice within this map, we used a combination of molecular dynamics simulations, X-ray crystallography, cross-linking mass spectrometry, and biophysics in an integrative structural biology approach. The Sap lattice model produced recapitulates a close-to-physiological arrangement, reveals high-resolution details of lattice contacts, and sheds light on the mechanisms underlying the stability of the Sap layer.**

S-layer | anthrax | cell surface | cryo-ET | exoskeleton

Significance

During exponential growth, *Bacillus anthracis*, the pathogen responsible for anthrax, is covered by the Sap S-layer, an outermost proteinaceous monolayer that is important for virulence and mechanical support to the cell envelope. Essential for these functions is the paracrystalline nature of the S-layer. We now present the complete atomic structure of in vitro grown Sap lattices. This model contains high-resolution details of lattice contacts and the mechanisms underlying the stability of the Sap layer, and suggests a conformational change from condensed monomers to postassembly protomers. The Sap lattice model helps explain how the S-layer forms and can be targeted with lattice-disrupting agents as potential therapeutics for the treatment of anthrax.

The surface layer or "S-layer" is a proteinaceous monolayer found to cover the entire cell surface in numerous Bacteria and almost all Archaea (1, 2). S-layers form paracrystalline arrays, typically consisting of a single secreted (glyco)protein that self-assembles to form a well-defined 2D lattice with specific symmetry (3). S-layer proteins (SLPs) are complex multidomain proteins that commonly contain a signal peptide (SP), a cell envelope binding module, and an assembly domain (AD) responsible for S-layer formation (2). In some organisms, the expression of SLPs is a resource-intensive process, accounting for 10% to 30% of total protein synthesis, making this envelope ultrastructure a significant part of the cell life cycle (4). Bacterial S-layers serve diverse functions, with alternative roles attributed in different organisms, including molecular sieving, modulation of infection, adhesion, protective coating, and more recently, acting as an exoskeleton (5–10). Due to their self-interacting nature, SLPs represent challenging structural targets, hampering three-dimensional crystallization and biophysical characterization. As a result, the current structural repertoire of SLPs remains scarce, often encompassing partial domains. In recent years, methodological advances are starting to provide atomic-level insights into S-layer structures, mapping their lattice contacts and arrangement on the cell surface (11–18).

Bacillus anthracis, a gram-positive and spore-forming bacterium, is the causative agent of anthrax—a zoonotic disease that primarily affects herbivorous animals. Anthrax remains a significant public health concern due to its high mortality rate despite antibiotic treatment (2% to >45% depending on infection route), the high environmental resilience of its spores and the absence of effective vaccination programs (19). The cell envelope of vegetative *B. anthracis* cells is characterized by the presence of an S-layer, composed of one of two mutually exclusive SLPs: Sap and EA1 (20, 21). The presence of an intact S-layer forms an important growth and virulence factor under environmental conditions and during infection (9, 14), making it an attractive therapeutic, vaccine, and diagnostic target (22, 23). While Sap is the dominant SLP during the exponential growth phase, cells switch to EA1 expression during the stationary phase in nutrient-rich media (24). Both S-layers have unique, noncompatible lattices (25), with Sap and EA1 coexisting only during the S-layer switch and then present in monomolecular patches (26). In *B. anthracis* and other S-layer-containing bacteria, S-layer assembly appears tightly regulated with cell expansion (26), suggesting a continuous S-layer is functionally important. Moreover, the use of Sap and EA1 depolymerizing nanobodies has shown that the crystallinity of the S-layer is

Author contributions: A.S., K.L., S.E.V.d.V., A.J.P., M.K., and H.R. designed research; A.S., K.L., E.V.H., S.E.V.d.V., and A.J.C. performed research; A.S. and A.F. contributed new reagents/analytic tools; A.S., K.L., E.V.H., S.E.V.d.V., A.J.C., A.F., A.J.P., M.K., and H.R. analyzed data; and A.S., K.L., S.E.V.d.V., A.J.P., M.K., and H.R. wrote the paper.

Competing interest statement: H.R. and A.F. are named as inventors on patent WO/2019/068677 describing the use of S-layer disrupting nanobodies as antibacterial agents. The other authors declare no competing interests.

This article is a PNAS Direct Submission.

[1]A.S., K.L., E.V.H., and S.E.V.d.V. contributed equally to this work.

[2]To whom correspondence may be addressed. Email: mikhail.kudryashev@mdc-berlin.de or han.remaut@vub.be.

This article contains supporting information online at https://www.pnas.org/lookup/suppl/doi:10.1073/pnas.2415351121/-/DCSupplemental.

Published December 9, 2024.

important for its function (14, 17). The acute disruption of Sap S-layer lattice integrity by nanobody treatment leaves behind an attached but amorphous layer of Sap, which results in severe morphological defects of the cell surface and eventual cell collapse (14). Similar observations were made in EA1, where stationary phase cells treated with lattice-disrupting nanobodies resulted in cell lysis under hypo-osmotic conditions (17). These remarkable observations suggest that under increased turgor pressure, the S-layer lattice is important for mechanical support of the cell envelope. Indeed, force nanoscopy showed that cells with a compromised Sap S-layer lattice exhibited decreased compressive stiffness and elastic modulus, providing compelling experimental evidence that the S-layer functions as a prokaryotic exoskeleton that promotes rigidity and mechanical stability to *B. anthracis* cell envelope (9). To fulfill this mechanical function, the S-layer relies on the noncovalent lateral crosslinking of subunits in the form of the S-layer lattice contacts.

The X-ray structure of the Sap assembly domain (Sap^{AD}) revealed the multidomain architecture of the protein, composed of six β-sandwich domains (D1 to D6) interconnected by short linkers (14) (Fig. 1*A*). An equivalent domain structure is seen in other S-layers known from *Bacillus* species, EA1, SbsB, and SbsC (13, 17, 27). In the stationary phase S-layer EA1, and in the *Geobacillus* S-layer SbsB, the solution state of the SLP monomers adopts a condensed structure that depends on the ordering of interdomain calcium binding sites. The supertertiary structures of these SLPs orient the domains into their assembly-competent conformations. Domains 3 to 6 adopt a flat tile-like architecture, with domains 1 and 2 protruding and forming a connection to the N-terminal domain that binds the peptidoglycan sacculus. In both proteins, the S-layer lattice assembles in a P1 symmetry by noncovalent protein–protein interactions between the SLP protomers. S-layer self-assembly takes minor rearrangements of the SLP protomer, primarily in the orientation of domains 1 and 2. The main *B. anthracis* S-layer Sap adopts a similarly condensed supertertiary structure, but one that does not depend on calcium binding.

To date, no clear insights exist into the intermolecular interactions in the Sap S-layer. The orientation and contact points of the Sap protomers within the lattice remain elusive, as well as the mechanism by which nanobodies dissolve the lattice and render the S-layer nonfunctional. To address these questions and obtain

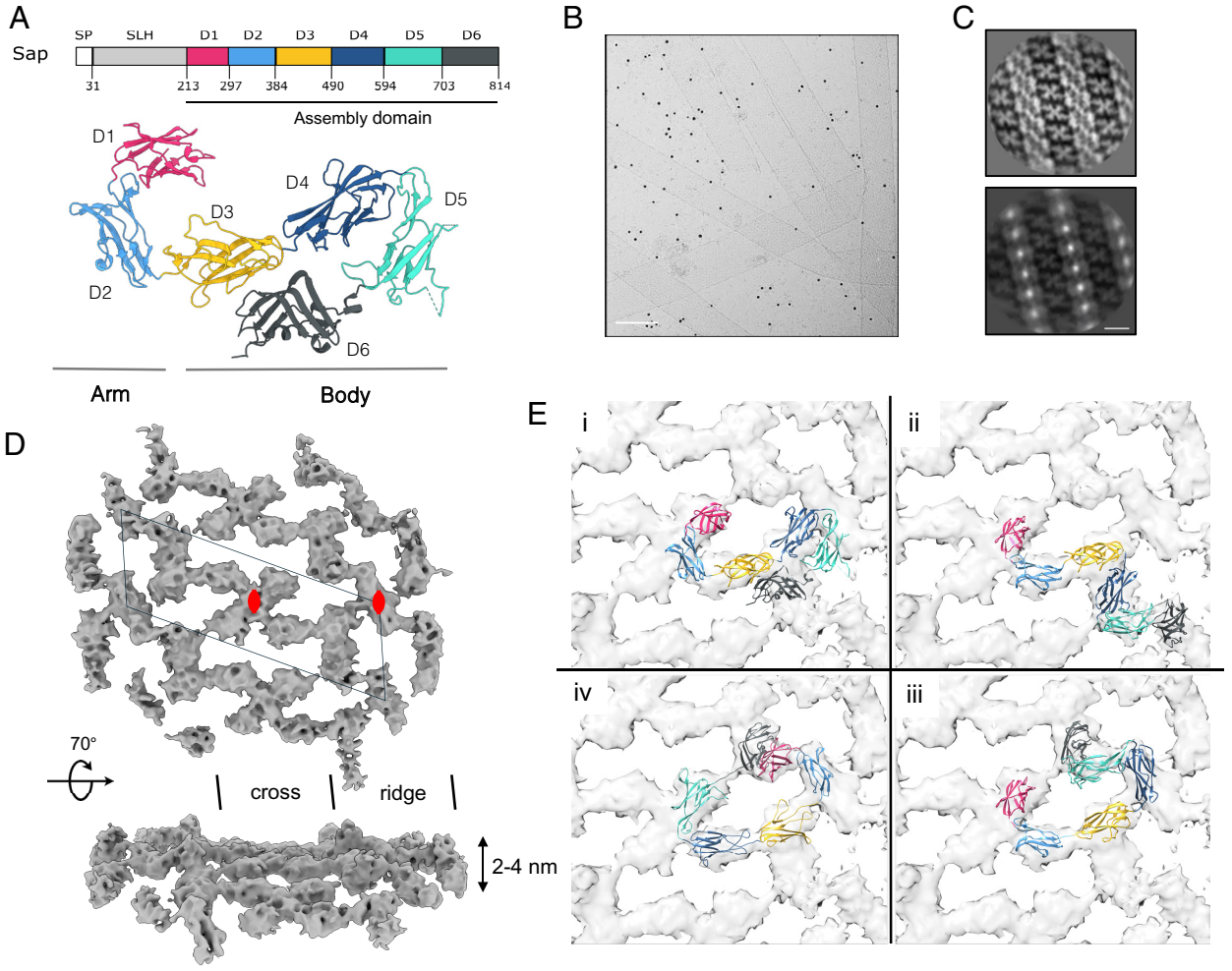

Fig. 1. Sap S-layer cryo-ET map and domain assignment ambiguity. (*A*) *Top*: Domain organization of Sap (SP: signal peptide; SLH: S-layer Homology domains; D1 to D6: Ig-like domains 1 to 2 in the S-layer AD). *Bottom*: Crystal structure of the Sap^{AD} (PDB 6HHU) in ribbon representation and colored by domains. Sap^{AD} domains give rise to an "Arm" (domains 1 and 2) and a "Body" (domains 3 to 6). (*B*) A cryo-EM micrograph of single-layered tubules of recombinant Sap^{AD}. (Scale bar, 100 nm.) (*C*) *Top*: 2D class average of in vitro assembled S-layers featuring a cross-and-ridge-like pattern with p2 symmetry. *Bottom*: 2D class average of Sap^{AD} S-layers labeled with Ni-NTA-nanogold. (*D*) Top and side views of the Sap^{AD} subtomogram average (StA) map at approximately 7.2-Å resolution. The map shows two two-fold symmetry points: one at the central cross-like region and the other at flanking ridge-like region, both indicated with red ovals. The dotted line shows the unit cell of the Sap S-layer lattice measuring a = 211.4 Å, b = 89.1 Å, γ = 84.0° (*E*) i) rigid body docking of the Sap^{AD} X-ray structure (PDB 6HHU) into the StA map. ii to iv) manually flexible body docked Sap monomers where D6 aligns with the ridge feature of the lattice, shown in ribbon representation and colored as in Fig. 1*A*.

a comprehensive model of the Sap S-layer lattice, we employed cryoelectron tomography (cryo-ET) and subtomogram averaging (StA) techniques to generate a medium-resolution map of in vitro reconstituted Sap S-layer. By integrating data from all-atom molecular dynamics simulations, with X-ray crystallography and biochemical experiments of domain–domain interfaces, we present a complete and experimentally validated model of the Sap S-layer lattice formed by the AD, with high-resolution information of the contact points within the lattice.

Results

Cryoelectron Tomography and Domain Docking of the Sap S-Layer. We previously showed that recombinant Sap^{AD} monomers (residues 214-814, i.e., missing the N-terminal, cell-wall-anchoring SLH domain) readily assemble into in vitro S-layers, forming 2D sheets and single-layered tubules with unit cell dimensions a = 211.4 Å, b = 89.1 Å, γ = 84.0°, values similar to those of the in vivo Sap S-layer as found on the *B. anthracis* cell surface (a = 184 Å, b = 81Å, γ = 84.0°) (14, 25). Two-dimensional (2D) classification and averaging of sections or "particles" cropped from electron micrographs of these in vitro-reconstituted S-layers resulted in classes featuring a cross-and-ridge-like pattern with p2 symmetry, reminiscent of the 2D crystallographic projection maps of in vivo S-layers (Fig. 1 *B* and *C*). To aid the positioning of the domains of the Sap to the lattice we labeled the N terminus of Sap with nanogold. Cryo-EM imaging followed by classification clearly put the N terminus in the middle of the "ridge" of the projection map. To obtain 3D structural information regarding the domain arrangement, preformed tubules of Sap^{AD} were prepared for cryo-ET (Fig. 1*D*). Tilt series of these tubules were recorded and tomograms were reconstructed for further analysis. Particles were cropped at regular intervals around the diameter and along the length of each tubule with the initial orientation defined as a normal to the tube. These tube segments were then iteratively aligned and averaged (*Materials and Methods*). The final StA reconstruction of Sap^{AD} (28) (applying C1 symmetry) had a resolution of 7.2 Å and was produced from 10,126 particles from 7 tomograms (Fig. 1*D* and *SI Appendix*, Fig. S1 *C* and *D* and Table S1).

The resulting map of the Sap lattice recapitulates the P2 symmetry seen in 2D projections, with two twofold protomer contacts in a central cross-like region and a flanking ridge-like region (Fig. 1*D*). The resulting map has an average height or "thickness" of ~2 nm, with a maximum of 4 nm in the ridges as a result of an outward protruding density. The map shows defined domain-like densities that match the dimensions of the beads-on-a-string Ig domains of the Sap monomer. However, the map resolution was insufficient to allow ab initio matching of any of the densities with individual Sap domains given the dominant β-stranded character of the Sap monomer structure. On first impression, the cross-like density is reminiscent of the D1D2 arm of the Sap^{AD}. However, the rigid body docking of the Sap^{AD} crystal structure demonstrates several mismatches in both the Sap^{AD} arm and body (D3 to D6), resulting in a poor overall correlation coefficient (cc) of the model and map (Fig. 1*E* model (i); cc = 0.509). This poor fit suggested the condensed solution state of the Sap^{AD} monomer [held monomeric by means of two bound nanobodies—not shown (14)] must undergo substantial conformational changes for the formation of the lattice.

The six Ig-like domains in the Sap^{AD} are connected by short linkers (3 to 7 residues). To generate a lattice model for Sap^{AD} consistent with the StA map, we explored multiple conformations by treating the individual domains (D1 to D6) as rigid bodies and allowing conformational rearrangements using the interdomain linkers as flexible hinge regions. To narrow down the plausible models, we mapped the location of the C-terminal hexahistidine tag on D6 by Ni-NTA-nanogold bead labeling and cryo-EM imaging followed by 2D class averaging. The strong density observed in the 2D classes corresponded to the gold beads and clearly aligned with the ridge feature of the lattice, away from the cross (Fig. 2*C*). Assuming the cross-like contact represents the D1D2 arm, two alternative flexible dockings of D3D4 are able to fit the density and place the D6 domain in the ridge region (Fig. 1*E*, models ii and iii; cc = 0.838 and 0.839, resp.). Alternatively, a flexible docking with D4D5 in the cross region is also able to place D6 in the ridge and give a reasonable fit of the densities in the StA map (Fig. 1*E*, model iv, cc = 0.891). The existence of at least three possible models that fit reasonably well within the StA map shows that the map alone does not allow unambiguous modeling of the Sap S-layer.

Molecular Dynamics Simulations of Sap Lattice Candidates. To iteratively construct, assess, and filter candidate S-layer models, we turned toward all-atom MD simulations. The first lattice model tested using MD (Fig. 2*A*) was derived from D1D2 forming the cross feature following the D1D2 atomic model from the X-ray monomer structure (PDB 6HHU) (14). The D3–D6 interface was extracted from the same X-ray structure. After 500 ns of simulation for each of the four independent replicas, we observed that the D4–D4 interface remained stable while the other three interfaces (D1D2–D1D2, D3–D6, D1–D5) fell apart, as indicated by either large changes in mean domain–domain distances or large SD (Fig. 2*A*). The next lattice model (Fig. 2*B*) was motivated by the stability of the D4–D4 interface, which we hypothesized to represent the cross feature instead of the unstable D1D2–D1D2 interface. However, in this layout, the lattice fell apart at all four interfaces (Fig. 2*B*). A third lattice model (Fig. 2*C*) was designed to avoid the interfaces that were identified as unstable in the prior two computational experiments, as well as the identification of p2 symmetric D2–D2 and D5–D5 interfaces that were predicted using Alphafold Multimer (29). Here, we first assumed that the D2–D2 interface formed the cross feature, yielding a ring-like Sap structure with D1 interacting with D6. We found that all four interfaces tended to dissociate. However, the D2–D2 interface remained associated in two of the four replica simulations, which suggested to us that the D2–D2 interface may still be viable for the next lattice model. The final lattice model (Fig. 2*D*) is equivalent to flex-dock model iv (Fig. 1*E*), where the cross feature is formed by a D5–D5 interface. Our simulations predict that all four interfaces in this lattice (D2–D2, D5–D5, D1–D6, D3–D6) are stable, although we did observe D2–D2 dissociation in one replica after ~300 ns (Fig. 2*D*). Finally, we note that the symmetric D2–D2 interface proved to be the most susceptible to strain due to the box length and was frequently the weak point of the lattice using the StA map-derived cell dimensions (*SI Appendix*, Fig. S1), which are 4.45% and 4.70% larger in the X and Y dimensions, respectively, compared to the optimal MD cell dimensions.

Experimental Validation of the Sap S-Layer Model. Motivated by the MD simulation results, we set out to validate model iv, in which the central cross is formed by D5–D5 interactions. This model contains three additional lattice contacts formed by D2–D2, D1–D6, and D3–D6. We studied the interaction of the two separately expressed heteromeric complex domains (D1–D6, D3–D6) using size exclusion chromatography. Purified D3 and D6 exhibited clear in vitro interaction, as evidenced by a shift to higher molecular weight (MW; Fig. 3*A*). While attempting to test the interaction between D1 and D6, we encountered solubility issues with recombinantly expressed D1. However, we successfully purified a construct comprising D1 and D2 (D1D2)

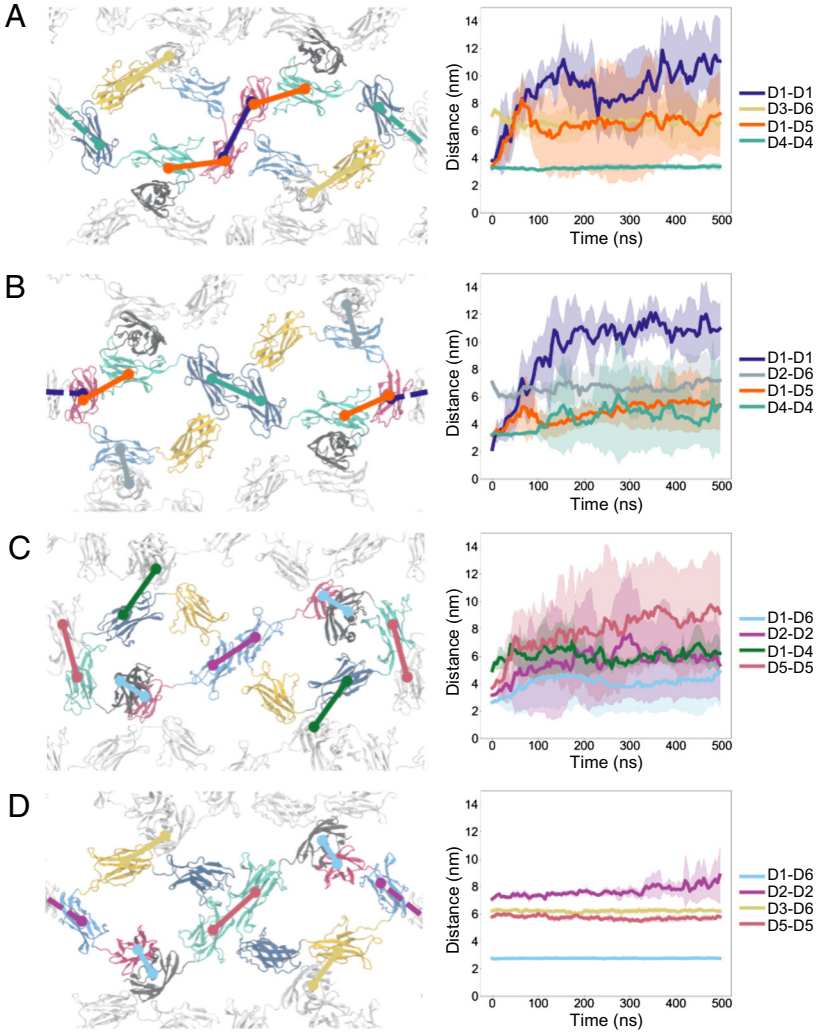

Fig. 2. Molecular dynamics assessment of candidate Sap lattices. (*A*–*D*) Model and time-series profiles depicting the mean distance (and SD with n = 4 or 8) between the centers-of-mass of each domain at the indicated interfaces for candidate lattice models where (*A*) D1D2, (*B*) D3D4, (*C*) D2D3, and (*D*) D4D5 represent the cross feature in the cryo-ET map. The snapshots (*Left*) depict the two Sap monomers (cartoon representation) in the unit cell, each composed of D1 (pink), D2 (light blue), D3 (yellow), D4 (dark blue), D5 (green), and D6 (gray). The solid lines overlaid on the snapshots represent the respective colors of each time-series profile (*Right*).

and confirmed its interaction with D6 through a higher MW shift in the size exclusion chromatography peak (Fig. 3*A*). Thus, these data corroborate the presence of stable D3–D6 and D1D2–D6 contacts, interactions not compatible with the Sap^{AD} solution state (Fig. 1*A*) and therefore candidate intermolecular contacts.

We next employed X-ray crystallography to obtain atomic resolution views of the interdomain contacts observed by SEC and predicted by the model iv simulation. We successfully crystallized D1D2–D1D2 (30), D3–D6 (31), and D4D5–D4D5 (32) domains (*SI Appendix*, Table S2). For an objective identification of the stable domain–domain contacts, PISA (Protein Interfaces, Surfaces, and Assemblies) was used to calculate interaction energies for all contacts in the crystals (33). In the D1D2–D1D2 crystal, the interface exhibiting the highest stability was formed by the interaction between D2 subunits (Fig. 3*B*). The D2 domains are involved in a twofold symmetric contact by β–β and side chain interactions of residues G356–T359 (Fig. 4). The D1D2–D1D2 dimer shows a good rigid body fit with the ridge region of the S-layer (cc = 0.86), where it coincides with the twofold axis in the lattice (Fig. 3*C*). Another two-fold symmetric interaction is seen in the D4D5–D4D5 crystals, formed by interaction of the D5 domains. The D4D5–D4D5 complex results in a distinctive interaction unit that gives a good rigid body fit (cc = 0.89) with the cross-like feature in the S-layer lattice, where it coincides with the second two-fold axis in the S-layer lattice (Fig. 3 *B* and *C*). Finally, the stable contact observed in the D3–D6 crystal corresponds to an asymmetric interaction, forming an intermolecular contact unit that shows a good rigid body fit with the residual density in the S-layer StA (cc = 0.89) (Fig. 3 *B* and *C*). When docked in the map, these individual complexes reconstitute the Sap^{AD} protomers with lattice contacts as found in model iv. Furthermore, these intermolecular contacts fit with the three stable interfaces identified in the MD simulations (model iv; Fig. 4*D*), suggesting they provide an atomic resolution view of the S-layer contacts. To further validate the S-layer model (34), mass spectrometry analysis of lysine crosslinking was conducted on monomer and polymer samples of Sap^{AD}. 115 observed crosslinks were mapped on the different candidate lattices using XlinkAnalyzer (35), with violations classified as a Cα–Cα distance of over 30 Å, a distance suitable for the BS-3 crosslinker (36). The D5–D5 cross candidate model showed the best consistency with the crosslinks, having less than 20% violations, with a few additional crosslinks just above the 30-Å threshold that could have been caused by small domain rearrangements not fully captured by the model (*SI Appendix*, Fig. S2). Notably, crosslinks validating the formed D3–D6–D1 (residues 437–773, 255–748), D45–D45 (509–645, 599–599, 599–692, 637–692), and D2–D2 (289–300, 344–344) interfaces were

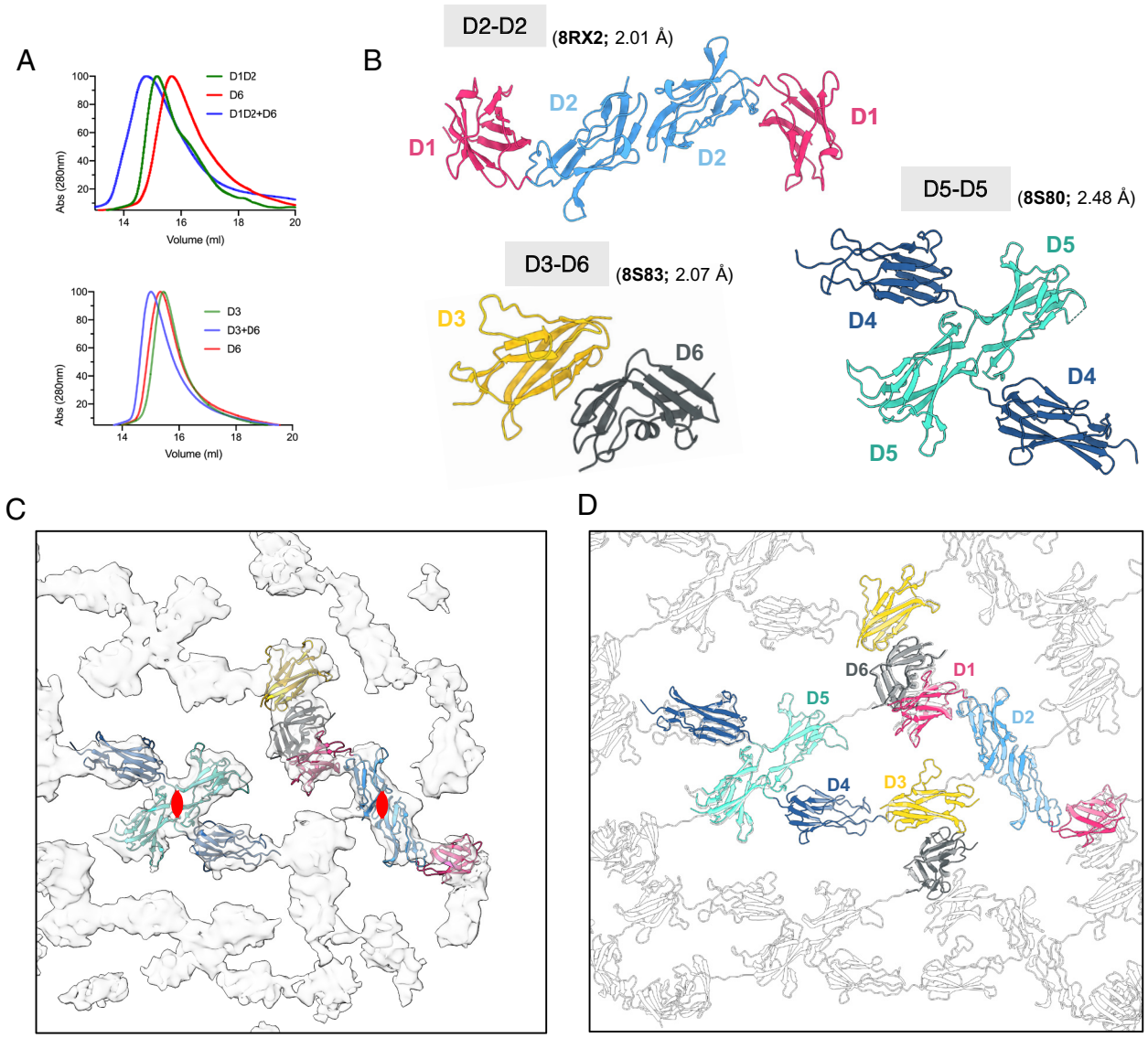

Fig. 3. Capturing Sap S-layer contacts by X-ray crystallography. (*A*) Size exclusion chromatogram (SEC) of the D1D2–D6 (*Top*) and D3–D6 (*Bottom*) heterocomplexes. Formation of the complex is confirmed by a shift to a smaller elution volume. (*B*) X-ray structures of domain–domain complexes capturing Sap S-layer interfaces. Resolution of the crystal structure and PDB code are indicated. (*C*) Rigid-body docking of domain–domain X-ray structures into the StA map. Red ovals indicated twofold symmetry axes. (*D*) Superimposition of Sap S-layer lattice model iv in ribbon representation (white), and the X-ray structures of domain–domain complexes (colored by domain).

overrepresented in the tubule-polymerized samples (*SI Appendix*, Table S3). The agreement between the X-ray structures, their rigid body fit with the StA map, the MD simulations, and the cross-linking reports provides compelling evidence for the validity of our proposed model and its ability to accurately capture the structural organization of the Sap S-layer.

Molecular Contact Points in the Sap Lattice. In the experimentally derived model of the Sap S-layer, Sap protomers would interact with four adjacent molecules via two twofold (D2–D2 and D5–D5) and two translational (D3–D6 and D1–D6) interactions (Fig. 4*A*). Three of these interfaces were captured in domain–domain crystal structures (Fig. 3 and *SI Appendix*, Table S2), providing atomic detail of their specific interactions. The D2–D2 interface maps to the ridge region of the S-layer, and involves a total surface area of 357.8 Å stabilized by 5 main chain (MC) and side chain (SC) hydrogen bonds through homotypic β-strand pairing ($Ser385^{MC}$–$Ser385^{MC}$, $Ser385^{SC}$–$Ser385^{SC}$, $Thr359^{SC}$–$Gly356^{MC}$, $Ser385^{MC}$–$Ser385^{MC}$, $Gly356^{MC}$–$Thr359^{SC}$) (Fig. 4 *B*, i). The cross-like region in the Sap lattice is composed of domains D4 and D5, where homotypic interactions of domain 5 form the primary contributor of the protomer–protomer interface. Notably, this interface features a central hydrophobic core consisting of phenylalanines complemented by four hydrogen bonds ($Phe597^{MC}$–$Leu693^{MC}$, $Lys637^{SC}$–$Asp690^{MC}$, $Leu693^{MC}$–$Phe597^{MC}$, $Asp690^{MC}$–$Lys637^{SC}$) and two salt bridges ($Lys637^{SC}$–$Asp690^{SC}$, $Asp690^{SC}$–$Lys637^{SC}$) (Fig. 4 *B*, ii). With a total surface area of 518 Å, the cross-like feature makes the largest domain–domain contact in the lattice and likely represents a major contributor to the stability and integrity of the S-layer. The third interface captured in our crystal structures involves domains D6 and D3. This interface is stabilized by five hydrogen bonds ($Thr445^{SC}$–$Gln801^{SC}$, $Lys452^{MC}$–$Ala759^{MC}$, $Thr761^{MC}$–$Asp451^{SC}$, $Thr761^{SC}$–$Asp451^{SC}$, and $Thr761^{SC}$–$Asp451^{SC}$) along with hydrophobic interactions, encompassing a total interface area of 431.6 Å (Fig. 4 *B*, iii). Notably, this intermolecular D3–D6 interface is isomorphous to the intramolecular D3–D6 contact previously reported for the $SapA^{AD}$ monomer in a condensed solution conformation (Fig. 5) (14).

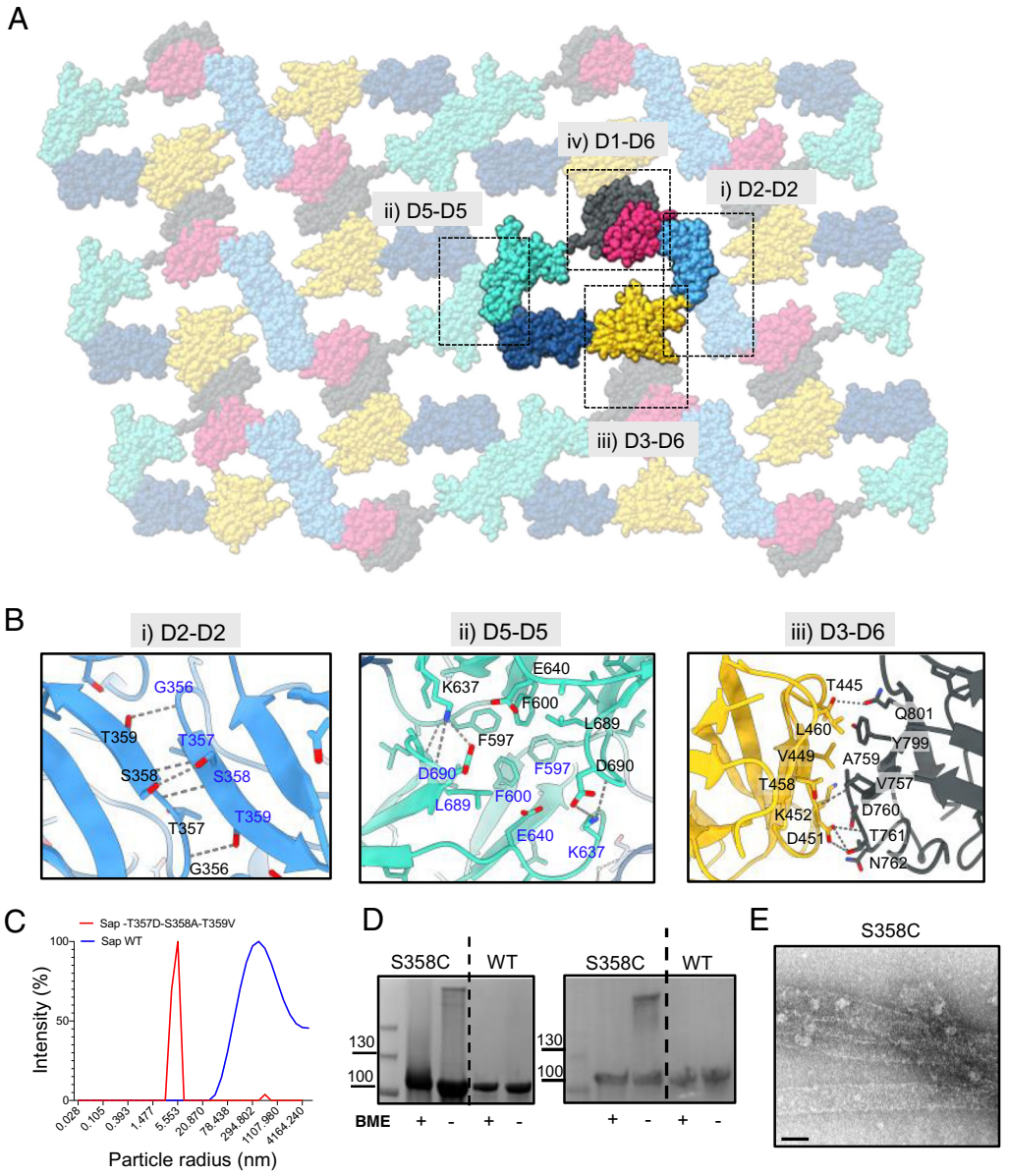

Fig. 4. Validation and atomic details of the Sap S-layer interfaces. (*A*) Complete Sap^{AD} S-layer model (domains 1 to 6) with atoms shown as spheres, colored by domain and with a central Sap monomer highlighted. The S-layer is stabilized by three inter- (labeled i to iii) and one intramolecular interaction (labeled iv), each boxed with a dotted line. (*B*) Atomic details of the lattice contacts of the Sap S-layer obtained by domain–domain X-ray crystallography. Residue labels of the homotypic complexes (D2–D2 and D5–D5) are labeled in gray and blue to distinguish both protomers. H-bonds are indicated as dotted gray lines. (*C*) Particle distribution and calculated hydrodynamic radius of Sap$^{FL\text{-}WT}$ and the mutant Sap$^{FL\text{-}T357D\text{-}S358A\text{-}T359V}$ as measured by dynamic light scattering (DLS). (*D*) Coomassie-stained SDS-PAGE (*Left*) and anti-Sap western blot (*Right*) of reduced (+) and nonreduced (−) Sap$^{FL\text{-}S358C}$ mutant, incorporating a cross-linking Cys at the D2 interface. Disulfide bonds formed in the mutants show Sap as higher molecular bands compared to the WT. BME: 2-mercaptoethanol. (*E*) Negative-staining TEM micrograph of in vitro reconstituted Sap$^{FL\text{-}S358C}$ mutant shows S-layer tubule formation. (Scale bar, 100 nm.)

To validate that the molecular contacts captured in the crystal structures indeed correspond to the lattice interfaces in the Sap S-layer we introduced point mutations at the D2–D2 interface. Specifically, we generated a lattice-breaking mutant by introducing two subtle substitutions (S358A and T359V) that would prevent the formation of three stabilizing hydrogen bonds, and introduced a charge repulsion by T357D mutation. The impact of the triple mutant (T357D–S358A–T359V) on lattice formation was then studied using DLS. While the mutant displayed a single population with a calculated hydrodynamic radius corresponding to the monomeric protein (Fig. 4*C*), the WT protein over time assembled into a broad range of high molecular weight species corresponding to in vitro S-layers. To ensure the lack-of-function of the T357D-S358A-T359V mutant was not due to indirect effects, we also sought positive confirmation by means of S358C as a candidate Cys–Cys crosslinking mutant across the D2 interface. In its native form, S358 forms a hydrogen bond with the corresponding S358 residue in the interacting monomer, with a distance of 3.21 Å (Fig. 4*B*). The formation of in vitro S-layers and the intermolecular cysteine crosslinking in the S358C mutant was monitored using negative stain EM and SDS-PAGE, respectively (Fig. 4 *D* and *E*). Purified Sap^{S385C} readily assembled into in vitro S-layers, and unlike WT Sap, it formed a redox-sensitive dimer upon S-layer assembly (i.e., in the presence of β-mercaptoethanol as reducing agent), confirming the presence and modeled interactions of the D2–D2 interface.

Dynamics of the Sap Interfaces by MD. After experimental validation of the Sap lattice model, we further analyzed the dynamics at each of the four domain–domain interfaces from our MD

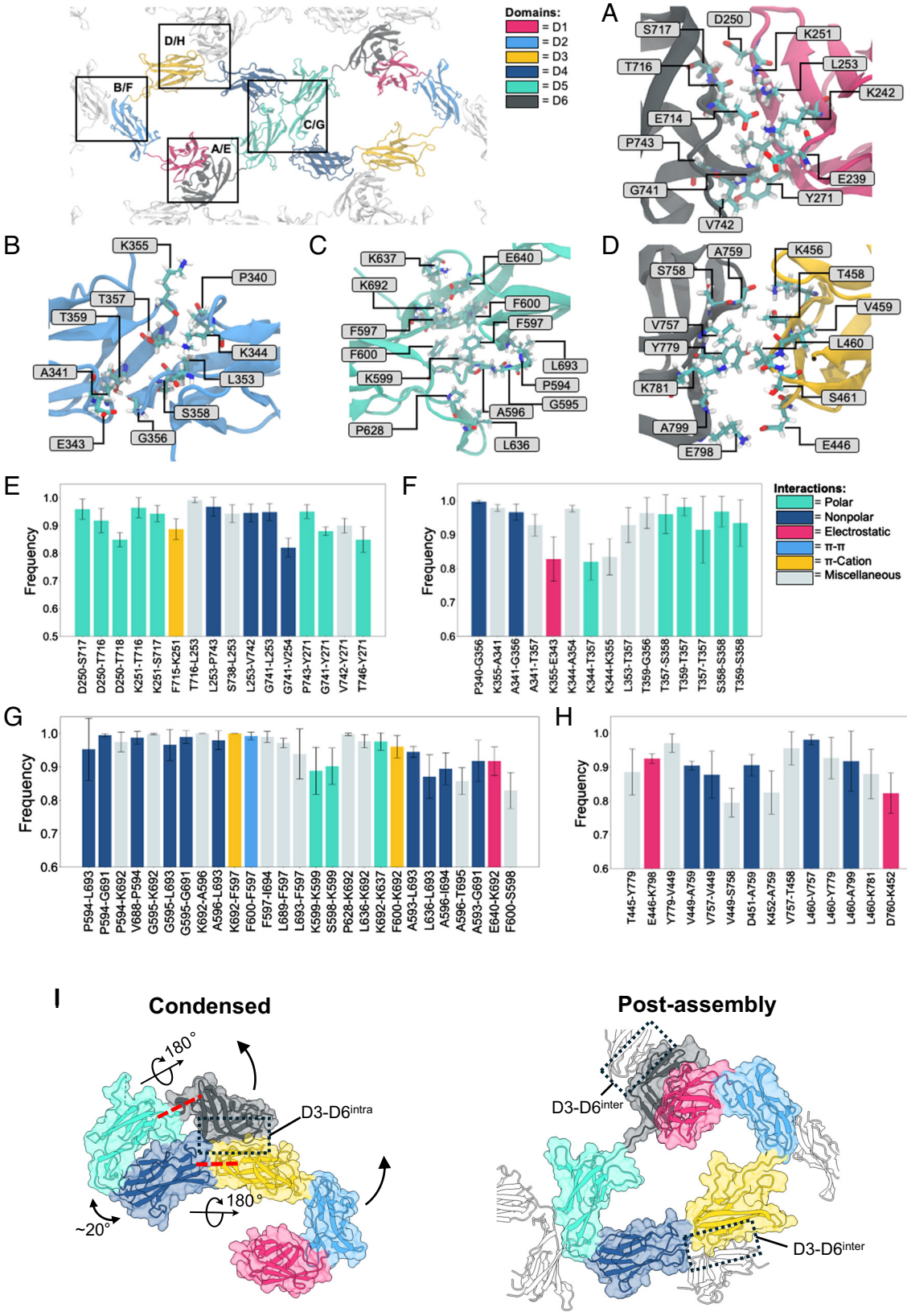

Fig. 5. Inter-Sap contact analysis by molecular dynamics simulations. (*A*–*D*) Snapshots depict the interfaces between (*A*) D1–D6, (*B*) D2–D2, (*C*) D5–D5, and (*D*) D3–D6. Domains are shown in cartoon representation (colored according to Fig. 1*A*), with interfacial residues depicted in stick representation and labeled. (*E* and *F*) Mean ± SD (n = 4) interfacial residue–residue contact frequency is shown for the interfaces between (*E*) D1–D6, (*F*) D2–D2, (*G*) D5–D5, and (*H*) D3–D6. Each bar is colored according to domain, which shows the type of interaction that is present. (*I*) Ribbon and surface representation of the $SapA^{AD}$ monomer (domains D1–D6) in condensed conformation (PDB 6HHU) and its postassembly S-layer conformation (this study; contacting domains of neighboring protomers shown in white). The pre- to postassembly transition involves a 20° pivoting around the D4–D5 linker and a rotational isomerization by 180° swivels of D6 and D3D2D1 around the flexible D5–D6 and D4–D3 linkers. The intramolecular D3–D6 contact is replaced by two isomorphous intermolecular D3–D6 contacts (boxed).

simulations (Fig. 5). First, we note that the D1–D6 interface was consistently the most stable across all four replicas. We find that the D1–D6 interface has sixteen identified interfacial residue–residue contacts, with ten contacts of frequency larger than 0.9 (Fig. 5 *A* and *E*). Comparison to the number of contacts at each interface suggests that this interface is one of the strongest throughout the lattice. Notably, the Thr716, Ser717, and Thr718 on D6 form stable interactions with Asp250 and Leu251 residues on D1 (Fig. 5*A*). While polar interactions are the most common type of interaction at this interface, nonpolar interactions between Leu253 and each of Gly741, Val742, and Pro743 are also notable. The symmetric D2–D2 interface has fifteen interfacial contacts, with eleven contacts of frequency larger than 0.9 (Fig. 5 *B* and *F*), suggesting that D2–D2 is another strong lattice interface. The main driving force for the stability of the D2–D2 interface is a sequence of Thr357-Ser358-Thr359 along an interfacial β-strand (Fig. 5*B*), the same sequence targeted in our lattice-breaking triple mutant. The hydrogen bonds formed by these residues with the corresponding β-strand across the interface are the most frequent and consistent; the breaking of these hydrogen bonds triggered the dissociation of the D2–D2 interface in one of the four replicas after ~300 ns (Fig. 2*D*). The other notable interactions on this strand are between Gly356 which formed nonpolar interactions with Pro340 and Ala341. The D5–D5 interface only has 9 domain–domain interfacial contacts but 18 linker–domain contacts, suggesting that this interface is potentially the strongest of all 4 and is largely mediated by linker–domain interactions (Fig. 5 *C* and *G*). At this interface, Lys692 forms a cation–π interaction with Phe600 and Phe597 and a salt bridge with Glu640, while Phe600 and Phe597 form a π–π interaction (Fig. 5*C*). Lys637 also forms a salt bridge with Asp690 and stable interactions with Gly691 and Lys692 at this interface (Fig. 5*C*). The interactions mediated by these lysine residues are also likely critical to the stability of the D5–D5 interface, which is consistent with the crosslinking data, with 338 observed crosslinks between Lys637 and Lys692, solely restricted to the polymer sample. Finally, the D3–D6 interface was the least stable across the four interfaces, as indicated by having only six interfacial contacts with a frequency above 0.9 and by the high SD across most contacts (Fig. 5 *D* and *H*). The key interactions that maintain this interface are likely the salt bridges between Glu446–Lys798 and possibly Lys452–Asp760. In addition, several nonpolar interactions, such as Leu460–Val757, are also present. In summary, we identify the interfaces with the largest number of interfacial contacts with high frequency as the most stable. D5–D5 is likely the most stable interface given the twenty-one identified contacts with frequency larger than 0.9. D1–D6 and D2–D2 have 10 and 11 contacts with frequency greater than 0.9, respectively, making these the next most stable interfaces throughout our current lattice model. D3–D6 has the fewest contacts with six greater than 0.9 frequency and is the least stable interface, especially given the much larger SD in contact frequency as compared to the three other interfaces.

Discussion

In this study, we have combined computational and experimental approaches to determine the structural organization of the Sap S-layer from the human and animal pathogen *B. anthracis*. We report a medium-resolution StA map of the Sap lattice, which revealed domain architecture that substantially differed from the monomeric structure previously reported in combination with a depolymerizing nanobody (PDB 6HHU). Since small angle X-ray scattering (SAXS) suggested the latter represents the conformation of the in-solution monomer (14), our map of the Sap lattice domain architecture implies Sap monomers undergo a substantial conformational change from the observed closed solution form to an open postassembly form. In the Sap monomer, intramolecular contacts between D4–D5 and D3–D6 give rise to a flat tile-shaped body (Figs. 1*A* and 5*I*), with domains D2 and D1 hanging off the body like an arm with an approximately 85° angle in the elbow. In the Sap S-layer, the intramolecular D4–D5 and D3–D6 contacts are broken to give way to the formation of a new intramolecular contact between D1 and D6 and four intermolecular lattice contacts, comprising homotypic D5–D5 and D2–D2 interactions and two isomerized D3–D6 and D6–D3 contacts (Fig. 5*I*). Remarkably, the disruption of the intramolecular D4–D5 and D3–D6 contacts results in an approximately 20° opening of the pivot angle between D4 and D5, and a 180° swivel of D6 and D3–D2–D1 around the D5–D6 and D3–D4 linkers, respectively. This rotational isomerization facilitates the formation of the new intramolecular contact between D1 and D6, and the formation of two new intermolecular D3–D6 contacts, which are otherwise isomorphous to the intramolecular D3–D6 contact (Fig. 5*I* and Movie S1). On the cell surface, Sap monomers emerge from the SEC translocon as unfolded chains. If and with what lifetime the condensed solution conformation of Sap monomers occurs in vivo, either as a competing off-route conformer or as a required intermediate to S-layer self-assembly is presently unclear. Our data illustrate the existence of competitive intra- and intermolecular D3–D6 contacts. In freshly purified samples, Sap is predominantly found as a monomeric species that self-assembles into Sap S-layers in a matter of hours (14), demonstrating that intra- and intermolecular D3–D6 contacts can interconvert, with the intermolecular Sap contacts as thermodynamic minimum. Strikingly, our MD simulations show the D3–D6 interface as the least stable across the four S-layer interfaces. The higher interdomain fluctuations at this interface, as compared to the other three interfaces, may be consistent with a required interconversion of the condensed solution form to the postassembly conformation. Although the individual contact points are limited in surface area, the overall S-layer structure demonstrates remarkable stability, readily forming even in solution. We propose that the high stability of the S-layer can be attributed to avidity, where the network of numerous weak interactions collectively contribute to the overall stability. We hypothesize that by relying on avidity of weaker domain-based interactions, the Sap S-layer is equipped with a delicate balance between stability and flexibility. Presumably this enables the S-layer to accommodate dynamic cellular processes, such as cell growth and division, while maintaining its structural integrity.

The emerging structures of SLPs found in the genus *Bacillus* reveal that despite their low pairwise sequence identity, these proteins adopt homologous beads-on-a-string domain structures that condense into a body (D3–D6) and arm (D1–D2) architecture (13, 14, 17, 27). A notable difference between Sap and SbsB, SbsC, and EA1 is that the latter three require calcium binding to adopt the assembly-competent conformation and form S-layers. In SbsB and EA1, the binding of 3 to 4 calcium ions structures intramolecular domain contacts that drive a conformational switch in domains D3–D6 from a linear conformational ensemble to a condensed tile-like body that exposes and shapes the interaction surfaces found in the S-layer contacts (13, 17). In Sap, this conformational switch does not implicate calcium binding, but rather the rotational isomerization of the intra- to an intermolecular D3–D6 contact. The reasons behind the deviation of Sap from a calcium-driven conformational switch are unknown, but may reflect the growth under low calcium concentrations, such as during intracellular germination of phagocytosed spores and the intracellular growth of *B. anthracis* during early infection.

Despite the architectural homology between *Bacillus* SLPs, each adopt unique lattices and lattice contacts. When comparing the Sap lattice to the other available S-layer structures, Sap shares the characteristic smooth surface to be presented toward the outside, while the protrusion of D1 in the ridge would connect to the cell-wall binding SLH domain (37) forming the corrugated side of the S-layer. However, the outward-facing surface of Sap is remarkably neutral compared to the other S-layers, which tend to be acidic, and as a group, the pI of S-layer assembly proteins tends to be acidic. Strikingly, Sap contains a large, irregular pore slit with approximate dimensions of 113 Å × 68 Å with the diameter reaching 30 to 40 Å in contrast with the tight lattices of *Clostridium difficile* and *Caulobacter crescentus*. Nevertheless, pore sizes of 2 to 8 nm are deemed canonical to S-layers, and pores of these dimensions would allow for a very permeable array being able to transport a wide range of molecules, from ions to even small folded proteins (7). These structural features suggest a potential role for the Sap S-layer in enabling dynamic molecular exchange and communication, including nutrient uptake, signaling, and potentially even the recognition of host molecules. To what extent the structural and topological differences in the various *Bacillus* S-layers alter their (selective) permeability to nutrients and proteins is largely unknown. With the availability of detailed S-layer models, we can also start to address the reasons underlying the metabolically costly exchange of S-layers seen in certain species, including *B. anthracis*. Finally, we anticipate that more S-layer models will allow the rationalization of the mechanical support given by S-layers and clarify the molecular mechanisms of S-layer disruptive antibodies.

Materials and Methods

Cloning for Recombinant Protein Production in *Escherichia coli*. Synthetic codon-optimized Sap_{AD} encompassing residues 216 to 814 (UniprotKB: P49051) with a C-terminal 6xHis tag was used from ref. 14. Full-length Sap (residues 31 to 814) was amplified from the *B. anthracis* (strain 34F2) genome using primers 383 and 384 and was subsequently cloned into linearized pASK-IBA3plus vector (using primers 321 and 322) by Gibson assembly and transformed into chemically competent DH5α *E. coli* (New England BioLabs). Construction of Sap mutants is described in Supplementary Methods, with all plasmid and primers used in this study listed in *SI Appendix*, Tables S4 and S5.

Protein Expression and Purification of Sap^{AD}, Sap^{FL}, and Sap Domains. Production and purification of the AD of Sap (Sap^{AD}: residues 216–814 with C-terminal His-tag, pAFSLP1) was conducted as previously described (14) and detailed in Supplementary Methods. Sap^{FL}, Sap^{FL} mutants, and individual Sap domains (all N-terminally tagged with 6xHis) were expressed in *E. coli* BL21 (DE3) grown in Terrific Broth (TB) supplemented with 100 μg/mL of Ampicillin at 37 °C and induced with 200 μg/L anhydrotetracycline when the OD_{600} reached 0.5. The different Sap forms were purified using Ni^{2+} IMAC and polished using size exclusion chromatography as described in *SI Appendix*, *Supplementary Methods*.

Sap^{AD} Tubule Formation and Sample Preparation for Cryo-ET. S-layer assembly was achieved by prolonged incubation at 25 °C of 2 mg/mL of freshly purified Sap^{AD} in PBS. Tubules were left to polymerize for 2 wk before being prepared for cryo-ET. For grid preparation, samples were mixed with concentrated 6-nm, gold-protein A conjugate (Aurion, 2.4^{13} particles per mL) for fiducials. The gold fiducials were concentrated by pelleting the stock solution for 45 min at >20,000×*g* in a benchtop centrifuge and pipetting off excess liquid to obtain more concentrated solutions in the manufacturer's storage buffer (PBS with 1% bovine serum albumin and 15 mM NaN_3). 2 μL of tubules was mixed with 8 μL of eightfold concentrated gold solution, after which 3 μL of the mixture was applied onto glow discharged UltrAuFoil R2/2 grids (Quantifoil), manually blotted in a CP3 Cryoplunge (Gatan) maintained close to 100% humidity at 22 °C, before being plunged in liquid ethane. Grids were stored in liquid nitrogen until used for screening or imaging by cryo-ET. Prior to high-resolution data collection, samples were screened at cryogenic temperatures using an in-house 120-kV JEM 1400 (JEOL) microscope equipped with a LaB_6 filament and a CMOS camera (TVIPS TemCam F-416).

Data Collection for Cryo-ET. Cryo-ET data collection was performed on a 300-kV Titan Krios G1 (FEI, ThermoFisher) equipped with a GIF Quantum® SE energy filter (Gatan) and K2 Summit direct electron detector (Gatan) at the Frankfurt Center for Electron Microscopy (FCEM), Goethe University Frankfurt. Data were collected in superresolution mode at a nominal magnification of 81,000×, corresponding to a pixel size of 0.9 Å, using a 70-μm objective aperture with defocus ranging from −2 to −3.5 μm. The dose-symmetric tilt scheme (38). Data collection was performed using SerialEM (39) to collect tilts between −60° and 60°, with 3° increments and a total exposure of ~156 e-/$Å^2$. Six superresolution frames were collected per tilt. For the first three tomograms, the zero-tilt image was collected with a high dose image of about 15 e-/$Å^2$ on camera, and the remaining dose was distributed equally over the nonzero tilts for the purposes of better visualization and incidental methods development.

Cryo-ET Image Processing and Subtomogram Averaging. Motion correction of the acquired movies was performed using MotionCor2 (40) and the resulting micrographs were assembled into a raw tilt series stack. Initial CTF correction was done using defocus estimation by Gctf (41) and ctfphaseflip from IMOD (42). Tilt series were aligned using gold fiducials manually. Tomograms were reconstructed from the collected tilt series using batch processing in IMOD (42).

Particles were picked and cropped from bin-8 tomograms using Dynamo Catalogue (43, 44). For this, we generated a supersampled mesh of crop-points defined along the length of each S-layer tube using the "Filament with rings" model along a manually defined central axis. As the tubes were of varying width (*SI Appendix*, Fig. S1*A*), the radius of each model was adjusted to the manually determined radius of the tube. Initial Euler angles of each particle were assigned as normal to the tube outer surface. Not all the tubes were perfectly round in cross-section, but rather appeared compressed to varying degrees by the ice layer (*SI Appendix*, Fig. S1*B*), so an initial box side-length of 48 pixels (nominally 345.6 Å) was chosen. This larger box size was chosen to 1) be sufficiently large to incorporate multiple pattern features observed in the 2D averages, and 2) be sufficiently large to accommodate larger z-shifts during refinement since cropping around an imagined circular cross-section on a compressed tube would result in some particles not being centered in the box. Two tomograms from the SAP-alone sample which had tubes with particularly round cross-sections were used to estimate a range of tube widths likely to have rounder tubules. Particles from these tubes (82 to 94 pixels, or nominally ~590.4 to 676.8 Å, in width) defined a subset of particles that were processed further.

An initial subset of the particles from a tomogram with round cross-sections was used to create an alignment project that started with a reference generated from a nonaligned average of 10% of the particles from this tomogram and went through two rounds of coarse alignment, each with three iterations. The result of this project was low-pass filtered to ~58 Å and used as the starting reference in a multireference alignment project of the width-subsetted bin-8 particles. Three classes were used to check the heterogeneity of the dataset. As all three classes looked similar to each other, all the particles were used going forward. Refinement with particle half sets was performed iteratively with gradually unbinning up to bin 2 (equivalent to a nominal counting resolution of 1.8 Å). A cylindrical half shell was used as the refinement mask at higher bin values and a shaped mask generated using RELION 3.1 (45) Mask Create was used later for lower bin values. Initial references were all filtered to at least 40 Å and in all stages, cross-correlation (cc) was used to include only the best 50% of the particles into the average.

At this point, in an effort to improve resolution further, 3D-CTF-corrected tomograms were generated using NovaCTF (46). Particles were recropped from these tomograms, re-refined from bin 4 to bin 2 (with half-sets still maintained) and recentered on the "X" cross. Finally, as the orientational coverage by the particles was good, to try to improve the resolution even further, 3D-CTF-corrected tomograms were reconstructed from only the −30° to 30° tilts and particles were recropped from these tomograms and subjected to a final round of refinement. Final resolutions were estimated by postprocessing in RELION 3.1 (45). Figures were created using ChimeraX (47).

Sap^{AD} Crosslinking and Mass Spectrometry Analysis. For crosslinking of Sap^{AD}, either freshly eluted monomeric material or two different batches of tubule material (>1 wk old) were subjected to crosslinking analysis and analyzed on

stain-free SDS-PAGE prior to mass spectrometry analysis. BS3 [bis(sulfosuccinimidyl)suberate, ThermoFisher] was dissolved in PBS (sample buffer) and reacted with either preformed tubules or monomeric Sap^{AD} in 20- or 50-fold molar excess of crosslinker. After 2 or 1 h, respectively, the reaction was quenched with 25 mM glycine and sent for trypsin digestion and mass spectrometry analysis at the VIB proteomics core (VIB, Ghent University). Given the complexity of the sample, i.e., a mix of monomer and polymer crosslinks in each sample, all crosslinks with occurrence >3 were selected for analysis regardless of their spread over different samples (for reference, *SI Appendix*, Table S3). Crosslinks were mapped and distance plots were generated for the different lattices using XlinkAnalyzer (35) as a plugin in Chimera (48), and 2D visualization was rendered using XiView (49). When lysines were not present in the structure file, the closest residue was taken for mapping (e.g., lysines 654, 810, 814).

Crystallization, Structure Determination, and analysis. Crystallization screens were set up using freshly purified domains. When two different domains were used, the molar ratio was 1:1. Samples were concentrated using AMICON 3-kDa MWCO centrifugal concentrators to various concentrations as indicated later. All crystals were obtained using the sitting drop vapor diffusion method and a Mosquito nanoliter-dispensing robot at room temperature (TTP Labtech, Melbourn, UK). First, optimal crystals of domain 1 and domain 2 appeared after 2 wk in a Morpheus kit condition containing 0.09 M halogens, 0.1 M buffer system 1 6.5 (pH) and 37.5% v/v Precipitant Mix 41 at 144 mg/mL. Crystals of the complex formed by domain 3 and domain 6 appeared after a week in a condition of the Proplex kit containing 0.1 M of sodium HEPES (pH 7.5) and 25% w/v PEG 2000 MME at 53 mg/mL. Diffracting crystals of the domains D4 and D5 appeared in a condition of the PACT screen containing 0.1 M MMT [malic acid, MES, and TRIS (1:2:2 molar ratio)], pH 7 and 25% w/v PEG 1,500 at 140 mg/mL after 10 d. In all cases, the drop containing the crystals was supplemented with 15% glycerol and the crystals were mounted in nylon loops and flash-cooled in liquid nitrogen. X-ray diffraction data were collected at 100 K using the Beamlines Proxima 2 and Proxima 1 at the Source optimisée de lumière d'énergie intermédiaire du LURE (SOLEIL) synchrotron (Gif-sur-Yvette, France) and beamline I04 at the Diamond Light Source (Didcot, UK). Data were processed with AutoProc (50) and XDS (51) and the structures were determined by molecular replacement using individual domains of the PDB 6HHU as a search model. The structures were refined through iterative cycles of manual model building with COOT (52) and reciprocal space refinement with phenix.refine (53) and Buster (54). All crystallographic statistics are shown in *SI Appendix*, Table S2. Study of the crystal interfaces was analyzed using the software PISA (33). Structural figures were generated with ChimeraX (47). Atomic coordinates and structure factors have been deposited in the protein data bank (PDB) under the accession codes: 8S83 (complex D3+D6), 8RX2 (homocomplex D1D2–D1D2), 8S80 (homocomplex D4D5).

All-Atom Molecular Dynamics Simulations. The X-ray atomic model of the Sap monomer was obtained from the Protein Data Bank (PDB) under the ID 6HHU. The PDB was processed using CHARMM-GUI (55) to replace engineered residues with canonical amino acids. Missing loops (residues 654–659 and residues 690–691) were filled using Modeller 10.1 (56). GROMACS 2021 (57) was then used to incorporate hydrogen atoms with standard protonation states. All simulations used the CHARMM36m force field (58).

Interfaces for the Sap protein lattice were aligned using domain–domain structures docked or predicted from HADDOCK 2.4 (59) or Alphafold Multimer v2.1.0, respectively (29). Docked structures were first manually positioned throughout the cryo-ET map based on each candidate lattice structure. Then, each domain of the complete Sap monomer was aligned via alpha-C atoms to the docked structures using visual molecular dynamics (VMD) (60). Energy minimization of the constructed dimeric structure was performed using steepest descent in vacuum using a buffer distance of 4 nm between all protein atoms and the box edges and a force tolerance of 1,000 kJ/mol/nm. Next, the energy-minimized dimer was placed in a triclinic box with dimensions of X = 85.1 Å, Y = 204.4 Å, Z = 10.0 Å, and $\gamma = 84°$. The system was subsequently neutralized with 0.15 M NaCl after solvation with water. Energy minimization was performed again with the same conditions as above. The four investigated lattice models contained 185, 235; 120, 617; 184, 917; 174, 740 atoms, respectively.

MD simulations were performed using GROMACS 2021 (57) and a timestep of 2 fs. Four replicas with identical initial coordinates and randomized velocities were initially run for 10 ns under constant NVT using the stochastic velocity rescaling thermostat (61) and a damping time of 0.1 ps, while all heavy atoms were restrained using a force constant of 1,000 kJ/mol/nm. An additional 85 ns was integrated to relax flexible regions of the protein and to allow side chains to reorient at protein–protein interfaces. This equilibration was done by adding a positional restraint (same force constant as before) to the C atoms outside 10 Å of any interface while allowing all interfacial residues and linkers to move freely. These trajectories were then extended with all positional restraints removed for longer production runs. We ran constant NVT dynamics for 500 ns using the same thermostat and a damping constant of 2.0 ps to test the stability of each interface in each proposed lattice model. Protein coordinates were extracted every 1 ns from each of the simulations for analysis. All trajectory analysis for dissociation and contact identification was done using the final 500 ns trajectories.

To analyze dissociation events, the distances between centers of mass of each interfacial domain were computed using MDTraj1.9.7 (62) and Contact Map Explorer 0.7.1 (63). The mean and SD for each relevant time-series distance profile was computed across all four replicas; the statistics for interfaces that appeared twice within a simulation (e.g., D3–D6) were considered independent samples, effectively yielding eight sets of data.

Interfacial contacts between protein residues were identified using a 4.5 Å cutoff between any heavy atom within each residue (64). Any residue–residue pair that satisfied this distance criteria was considered a contact while its frequency was calculated by normalizing the number of frames with successful contacts by the total number of frames in the trajectory. The mean and SD of each contact frequency was computed from four replicas and any residue pairs with frequency greater than 0.75 were identified as stable interfacial contacts. Snapshots of interfacial structures were generated using VMD (60).

Data, Materials, and Software Availability. The atomic coordinates of the domain–domain X-ray structures have been deposited in the Protein Data Bank (PDB) with the accession codes: 8S83 (D3–D6) (31), 8RX2 (D1–D2) (30), and 8S80 (D4–D5) (32). The final model has been deposited in the PDB with accession code: 9G93 (34). The StA map been deposited in the EMDB with accession code: EMD-45459 (28). All other data are included in the manuscript and/or supporting information.

ACKNOWLEDGMENTS. This work was partially supported by Vlaams Instituut voor Biotechnologie (VIB) and Fonds voor Wetenschappelijk Onderzoek (FWO) Flanders through project Grant No. G065220N. A.F. was supported by a postdoctoral fellowship from FWO (1253121N). A.S. was supported by the European Molecular Biology Organization (EMBO-ALTF-709-2021) and the Marie Skłodowska-Curie Actions (MSCA) MSCA-SLYDIV project. K.L. and M.K. were funded by the Sofja Kovalevskaja Award from the Alexander von Humboldt Foundation. M.K. is supported by the Heisenberg Award from Deutsche Forschungsgemeinschaft and by the Helmholtz Society. E.V.H., A.J.C., and A.J.P. were supported by the National Institute of Allergy and Infectious Diseases of the NIH under Award No. R21AI168838. We thank Bio Electron Cryogenic Microscopy (BECM) and Dr. Marcus Fislage for his assistance during cryo-EM data collection. We thank the staff of the synchrotron SOLEIL and Diamond for assistance and support in using their beamlines. We thank Deryck Mills for his assistance with (and assiduous maintenance of) the microscopes as well as Dr. Özkan Yildiz and Dr. Juan Castillo-Hernandez for their Information Technology support at the Max Planck Institute of Biophysics. We acknowledge the use of high-performance computing resources from the Cyber Infrastructure & Advanced Research Computing Group at Colorado School of Mines and through allocation BIO220015 from the Advanced Cyberinfrastructure Coordination Ecosystem: Services & Support program, which is supported by NSF Grants #2138259, #2138286, #2138307, #2137603, and #2138296.

Author affiliations: [a]Structural and Molecular Microbiology, Vlaams Instituut voor Biotechnologie (VIB)-Vrije Universiteit Brussel (VUB) Center for Structural Biology, Vlaams Instituut voor Biotechnologie, Brussels 1050, Belgium; [b]Structural Biology Brussels, Department for Bio-engineering Sciences, Vrije Universiteit Brussel, Brussels 1050, Belgium; [c]Max Planck Institute of Biophysics, Frankfurt on Main 60438, Germany; [d]Buchmann Institute for Molecular Life Sciences, Goethe University of Frankfurt on Main, Frankfurt 60438, Germany; [e]In Situ Structural Biology, Max Delbrück Center for Molecular Medicine in the Helmholtz Association, Berlin 13092, Germany; [f]Institute of Medical Physics and Biophysics, Charité-Universitätsmedizin Berlin, Berlin 10117, Germany; [g]Chemical and Biological Engineering, Colorado School of Mines, Golden, CO 80401; [h]Quantitative Biosciences and Engineering, Colorado School of Mines, Golden, CO 80401; and [i]Materials Science Program, Colorado School of Mines, Golden, CO 80401

1. U. B. Sleytr, B. Schuster, E. M. Egelseer, D. Pum, S-layers: Principles and applications. *FEMS Microbiol. Rev.* **38**, 823–864 (2014).
2. R. P. Fagan, N. F. Fairweather, Biogenesis and functions of bacterial S-layers. *Nat. Rev. Microbiol.* **12**, 211–222 (2014).
3. D. Pum, A. Breitwieser, U. B. Sleytr, Patterns in nature–S-layer lattices of bacterial and archaeal cells. *Crystals* **11**, 869–886 (2021).
4. J. H. Lau, J. F. Nomellini, J. Smit, Analysis of high-level S-layer protein secretion in *Caulobacter crescentus*. *Can. J. Microbiol.* **56**, 501–514 (2010).
5. A. Chandramohan *et al.*, Novel mechanism for surface layer shedding and regenerating in bacteria exposed to metal-contaminated conditions. *Front. Microbiol.* **9**, 3210–3210 (2019).
6. M. J. Blaser, P. F. Smith, J. E. Repine, K. A. Joiner, Pathogenesis of *Campylobacter* fetus infections. Failure of encapsulated *Campylobacter* fetus to bind C3b explains serum and phagocytosis resistance. *J. Clin. Invest.* **81**, 1434–1444 (1988).
7. M. Sára, U. B. Sleytr, Molecular sieving through S layers of *Bacillus stearothermophilus* strains. *J. Bacteriol.* **169**, 4092–4098 (1987).
8. S. F. Koval, S. H. Hynes, Effect of paracrystalline protein surface layers on predation by *Bdellovibrio bacteriovorus*. *J. Bacteriol.* **173**, 2244–2249 (1991).
9. A. Fioravanti, M. Mathelie-Guinlet, Y. F. Dufrene, H. Remaut, The *Bacillus anthracis* S-layer is an exoskeleton-like structure that imparts mechanical and osmotic stabilization to the cell wall. *PNAS Nexus* **1**, pgac121 (2022).
10. E. Gerbino, P. Carasi, P. Mobili, M. A. Serradell, A. Gómez-Zavaglia, Role of S-layer proteins in bacteria. *World J. Microbiol. Biotechnol.* **31**, 1877–1887 (2015).
11. T. A. M. Bharat, A. von Kügelgen, V. Alva, Molecular logic of prokaryotic surface layer structures. *Trends Microbiol.* **29**, 405–415 (2021).
12. M. A. Arbing *et al.*, Structure of the surface layer of the methanogenic archaean *Methanosarcina acetivorans*. *Proc. Natl. Acad. Sci. U.S.A.* **109**, 11812–11817 (2012).
13. E. Baranova *et al.*, SbsB structure and lattice reconstruction unveil Ca^{2+} triggered S-layer assembly. *Nature* **487**, 119–122 (2012).
14. A. Fioravanti *et al.*, Structure of S-layer protein Sap reveals a mechanism for therapeutic intervention in anthrax. *Nat. Microbiol.* **4**, 1805–1814 (2019).
15. A. von Kugelgen *et al.*, Interdigitated immunoglobulin arrays form the hyperstable surface layer of the extremophilic bacterium *Deinococcus radiodurans*. *Proc. Natl. Acad. Sci. U.S.A.* **120**, e2215808120 (2023).
16. A. von Kugelgen *et al.*, In situ structure of an intact lipopolysaccharide-bound bacterial surface layer. *Cell* **180**, 348–358 e315 (2020).
17. A. Sogues *et al.*, Structure and function of the EA1 surface layer of *Bacillus anthracis*. *Nat. Commun.* **14**, 7051 (2023).
18. L. Gambelli *et al.*, Structure of the two-component S-layer of the archaeon *Sulfolobus acidocaldarius*. *eLife* **13**, e84617 (2024).
19. K. A. Hendricks *et al.*, Centers for disease control and prevention expert panel meetings on prevention and treatment of anthrax in adults. *Emerg. Infect. Dis.* **20**, e130687 (2014).
20. A. Fouet, The surface of *Bacillus anthracis*. *Mol. Aspects Med.* **30**, 374–385 (2009).
21. A. Chateau, S. E. Van der Verren, H. Remaut, A. Fioravanti, The Bacillus anthracis cell envelope: Composition, physiological role, and clinical relevance. *Microorganisms* **8**, 1864 (2020).
22. Y. Zhang *et al.*, Plasmid-based vaccination with candidate anthrax vaccine antigens induces durable type 1 and type 2 T-helper immune responses. *Vaccine* **26**, 614–622 (2008).
23. A. A. Zasada, Detection and identification of *Bacillus anthracis*: From conventional to molecular microbiology methods. *Microorganisms* **8**, 125 (2020).
24. T. Mignot, S. Mesnage, E. Couture-Tosi, M. Mock, A. Fouet, Developmental switch of S-layer protein synthesis in *Bacillus anthracis*. *Mol. Microbiol.* **43**, 1615–1627 (2002).
25. E. Couture-Tosi *et al.*, Structural analysis and evidence for dynamic emergence of *Bacillus anthracis* S-layer networks. *J. Bacteriol.* **184**, 6448–6456 (2002).
26. V. J. Kern, J. W. Kern, J. A. Theriot, O. Schneewind, D. Missiakas, Surface-layer (S-layer) proteins sap and EA1 govern the binding of the S-layer–associated protein BslO at the cell septa of *Bacillus anthracis*. *J. Bacteriol.* **194**, 3833–3840 (2012).
27. T. Pavkov *et al.*, The structure and binding behavior of the bacterial cell surface layer protein SbsC. *Structure* **16**, 1226–1237 (2008).
28. K. E. Leigh, S. E. Van der Verren, H. Remaut, M. Kudryashev, Structure of in vitro assembled B. anthracis S-layer protein Sap. EMD. https://www.ebi.ac.uk/emdb/EMD-45459. Deposited 22 July 2024.
29. R. Evans *et al.*, Protein complex prediction with AlphaFold-Multimer. bioRxiv [Preprint] (2022). https://doi.org/10.1101/2021.10.04.463034 (Accessed 10 March 2022).
30. A. Sogues, H. Remaut, Domains 1 and 2 of Sap S-layer protein from *Bacillus anthracis*. RCSB PDB. https://www.rcsb.org/structure/8RX2. Deposited 6 February 2024.
31. A. Sogues, H. Remaut, Domains 3 and 6 of Sap S-layer protein from *Bacillus anthracis*. https://www.rcsb.org/structure/8S83. RCSB PDB. Deposited 5 March 2024.
32. A. Sogues, H. Remaut, Domains 4 and 5 of Sap S-layer protein from *Bacillus anthracis*. RCSB PDB. https://www.rcsb.org/structure/8S80. Deposited 5 March 2024.
33. E. Krissinel, K. Henrick, Inference of macromolecular assemblies from crystalline state. *J. Mol. Biol.* **372**, 774–797 (2007).
34. A. Sogues *et al.*, CryoET structure of the in vitro grown *Bacillus anthracis* Sap S-layer. RCSB PDB. https://www.rcsb.org/structure/9G93. Deposited 24 July 2024.
35. J. Kosinski *et al.*, Xlink Analyzer: Software for analysis and visualization of cross-linking data in the context of three-dimensional structures. *J. Struct. Biol.* **189**, 177–183 (2015).
36. E. D. Merkley *et al.*, Distance restraints from crosslinking mass spectrometry: Mining a molecular dynamics simulation database to evaluate lysine–lysine distances. *Protein Sci.* **23**, 747–759 (2014).
37. D. Sychantha *et al.*, Molecular basis for the attachment of S-layer proteins to the cell wall of *Bacillus anthracis*. *Biochemistry* **57**, 1949–1953 (2018).
38. W. J. H. Hagen, W. Wan, J. A. G. Briggs, Implementation of a cryo-electron tomography tilt-scheme optimized for high resolution subtomogram averaging. *J. Struct. Biol.* **197**, 191–198 (2017).
39. D. N. Mastronarde, Automated electron microscope tomography using robust prediction of specimen movements. *J. Struct. Biol.* **152**, 36–51 (2005).
40. S. Q. Zheng *et al.*, MotionCor2: Anisotropic correction of beam-induced motion for improved cryo-electron microscopy. *Nat. Methods* **14**, 331–332 (2017).
41. K. Zhang, Gctf: Real-time CTF determination and correction. *J. Struct. Biol.* **193**, 1–12 (2016).
42. D. N. Mastronarde, S. R. Held, Automated tilt series alignment and tomographic reconstruction in IMOD. *J. Struct. Biol.* **197**, 102–113 (2017).
43. D. Castano-Diez, M. Kudryashev, M. Arheit, H. Stahlberg, Dynamo: A flexible, user-friendly development tool for subtomogram averaging of cryo-EM data in high-performance computing environments. *J. Struct. Biol.* **178**, 139–151 (2012).
44. D. Castano-Diez, M. Kudryashev, H. Stahlberg, Dynamo catalogue: Geometrical tools and data management for particle picking in subtomogram averaging of cryo-electron tomograms. *J. Struct. Biol.* **197**, 135–144 (2017).
45. S. H. Scheres, RELION: Implementation of a Bayesian approach to cryo-EM structure determination. *J. Struct. Biol.* **180**, 519–530 (2012).
46. B. Turonova, F. K. M. Schur, W. Wan, J. A. G. Briggs, Efficient 3D-CTF correction for cryo-electron tomography using NovaCTF improves subtomogram averaging resolution to 3.4A. *J. Struct. Biol.* **199**, 187–195 (2017).
47. E. C. Meng *et al.*, UCSF ChimeraX: Tools for structure building and analysis. *Protein Sci.* **32**, e4792 (2023).
48. E. F. Pettersen *et al.*, UCSF Chimera–A visualization system for exploratory research and analysis. *J. Comput. Chem.* **25**, 1605–1612 (2004).
49. C. W. Combe, M. Graham, L. Kolbowski, L. Fischer, J. Rappsilber, xiVIEW: Visualisation of crosslinking mass spectrometry data. *J. Mol. Biol.* 436, 168656 (2024). https://doi.org/10.1016/j.jmb.2024.168656.
50. C. Vonrhein *et al.*, Data processing and analysis with the autoPROC toolbox. *Acta Crystallogr. D, Biol. Crystallogr.* **67**, 293–302 (2011).
51. W. Kabsch, Xds. *Acta Crystallogr. D, Biol. Crystallogr.* **66**, 125–132 (2010).
52. P. Emsley, K. Cowtan, Coot: Model-building tools for molecular graphics. *Acta Crystallogr. D, Biol. Crystallogr.* **60**, 2126–2132 (2004).
53. P. V. Afonine *et al.*, Towards automated crystallographic structure refinement with phenix.refine. *Acta Crystallogr. D, Biol. Crystallogr.* **68**, 352–367 (2012).
54. O. S. Smart *et al.*, Exploiting structure similarity in refinement: Automated NCS and target-structure restraints in BUSTER. *Acta Crystallogr. D, Biol. Crystallogr.* **68**, 368–380 (2012).
55. S. Jo, T. Kim, V. G. Iyer, W. Im, CHARMM-GUI: A web-based graphical user interface for CHARMM. *J. Comput. Chem.* **29**, 1859–1865 (2008).
56. A. Sali, T. L. Blundell, Comparative protein modelling by satisfaction of spatial restraints. *J. Mol. Biol.* **234**, 779–815 (1993).
57. B. Hess, C. Kutzner, D. van der Spoel, E. Lindahl, GROMACS 4: Algorithms for highly efficient, load-balanced, and scalable molecular simulation. *J. Chem. Theory Comput.* **4**, 435–447 (2008).
58. J. Huang *et al.*, CHARMM36m: An improved force field for folded and intrinsically disordered proteins. *Nat. Methods* **14**, 71–73 (2017).
59. G. C. P. van Zundert *et al.*, The HADDOCK2.2 web server: User-friendly integrative modeling of biomolecular complexes. *J. Mol. Biol.* **428**, 720–725 (2016).
60. W. Humphrey, A. Dalke, K. Schulten, VMD: Visual molecular dynamics. *J. Mol. Graph.* **14**, 27–38 (1996).
61. G. Bussi, T. Zykova-Timan, M. Parrinello, Isothermal-isobaric molecular dynamics using stochastic velocity rescaling. *J. Chem. Phys.* **130**, 074101 (2009).
62. R. T. McGibbon *et al.*, MDTraj: A modern open library for the analysis of molecular dynamics trajectories. *Biophys. J.* **109**, 1528–1532 (2015).
63. D. W. H. Swenson, S. Roet, *Contact Map Explorer Source Code (Version 0.7.1)* (2021).
64. R. B. Best, G. Hummer, W. A. Eaton, Native contacts determine protein folding mechanisms in atomistic simulations. *Proc. Natl. Acad. Sci. U.S.A.* **110**, 17874–17879 (2013).